The influence of oxygen partial pressure on material properties of Eu3+−doped Y2O2S thin film deposited by Pulsed Laser Deposition

Article *in* Physica B Condensed Matter · October 2015

DOI: 10.1016/j.physb.2015.10.005

3 authors:

Abdub Guyo Ali

University of the Free State

6 PUBLICATIONS **19** CITATIONS

SEE PROFILE

Francis Dejene

University of the Free State

25 PUBLICATIONS **85** CITATIONS

SEE PROFILE

H. C. Swart

University of the Free State

528 PUBLICATIONS **3,327** CITATIONS

SEE PROFILE

Physica B 480 (2016) 174–180

Contents lists available at ScienceDirect

Physica B

journal homepage: www.elsevier.com/locate/physb

The influence of oxygen partial pressure on material properties of Eu^{3+}-doped Y_2O_2S thin film deposited by Pulsed Laser Deposition

A.G. Ali [a,*], B.F. Dejene [a], H.C. Swart [b]

[a] Department of Physics, University of the Free State (Qwaqwa Campus), Private Bag X13, Phuthaditjhaba 9866, South Africa
[b] Department of Physics, University of the Free State, P.O. Box 339, Bloemfontein 9300, South Africa

ARTICLE INFO

Article history:
Received 3 July 2015
Received in revised form
23 September 2015
Accepted 1 October 2015
Available online 9 October 2015

Keywords:
Thin film
Phosphor
$Y_2O_2S:Eu^{3+}$
PLD
XRD
PL

ABSTRACT

Eu^{3+}-doping has been of interest to improve the luminescent characteristics of thin-film phosphors. $Y_2O_2S:Eu^{3+}$ films have been grown on Si (100) substrates by using a Pulsed Laser Deposition technique. The thin films grown under different oxygen deposition pressure conditions have been characterized using structural and luminescent measurements. The X-ray diffraction patterns showed mixed phases of cubic and hexagonal crystal structures. As the oxygen partial pressure increased, the crystallinity of the films improved. Further increase of the O_2 pressure to 140 mtorr reduced the crystallinity of the film. Similarly, both scanning electron microscopy and Atomic Force Microscopy confirmed that an increase in O_2 pressure affected the morphology of the films. The average band gap of the films calculated from diffuse reflectance spectra using the Kubelka–Munk function was about 4.75 eV. The photoluminescence measurements indicated red emission of $Y_2O_2S:Eu^{3+}$ thin films with the most intense peak appearing at 619 nm, which is assigned to the $^5D_0$–$^7F_2$ transition of Eu^{3+}. This most intense peak was totally quenched at higher O_2 pressures. This phosphor may be a promising material for applications in the flat panel displays.

1. Introduction

Europium-doped Y_2O_2S exhibits strong UV and cathode ray-excited luminescence, so it is widely used as red phosphors for low-pressure fluorescent lamps, cathode-ray tubes and plasma display panels (PDPs) [1]. Also, the hexagonal Y_2O_2S is a good host material for rare earth ions. A lot of attention has been given to the nanoscale $Y_2O_2S:Eu^{3+}$ for its tremendous potential applications in optical display and lighting materials and basic science research on special luminescent spectra [2–4]. Nanoscale $Y_2O_2S:Eu^{3+}$ has remarkably different luminescent properties from those of bulk samples: such as emission line broadening, lifetime changes and its spectral shift [5]. There are several methods to synthesize nanocrystalline $Y_2O_2S:Eu^{3+}$, such as sol–gel [6], combustion [7], micro-emulsion [8], and spray pyrolysis method [9], but these methods are limited in the complexity of the preparation methods. Solid state reaction at room temperature is a good method to synthesize nanoparticles [10–12]. It is generally accepted that thin-film phosphors have several advantages over bulk-type powder phosphors: better thermal stability, reduced outgassing, better adhesion, and improved uniformity over substrate surface. However, the biggest hindrance in the application of thin-film phosphors is their low brightness and efficiency in comparison to those of powder phosphors. Pulsed laser deposition (PLD) technique, which provides a unique process for stoichiometric evaporation of target materials and control of film morphology [13,14], has been used for the deposition of oxysulfide films [15–17].

In this work, we report on a study of the PLD conditions, the consequent crystalline and surface morphology structures, and photoluminescence (PL) characteristics of $Y_2O_2S:Eu^{3+}$ thin films. Our study showed that the oxygen partial pressure positively affected the crystalline phase, the morphology and the PL efficiency of the thin films. The luminescence results show that the PL intensity from $Y_2O_2S:Eu^{3+}$ films under oxygen partial pressure may be as much as 1.4 times higher than that from $Y_2O_2S:Eu^{3+}$ film deposited in vacuum. As far as our knowledge is concerned, no one has so far investigated the influence of oxygen partial pressure of material properties of $Y_2O_2S:Eu^{3+}$ under these conditions and achieved similar results.

2. Experimental procedure

2.1. Powder synthesis

$Y_2O_2S:Eu^{3+}$ nanocrystals were synthesized using the sol-combustion route. The method of synthesis essentially comprises

* Corresponding author. Fax: +27 58 718 5444.
E-mail address: aliag@qwa.ufs.ac.za (A.G. Ali).

http://dx.doi.org/10.1016/j.physb.2015.10.005
0921-4526/

of mixing the precursors in appropriate stoichemetric ratios, followed by firing in an air tube furnace at a temperature of 500 °C. The white foamy product was then grounded and left to dry in an enclosed oven for 24 h. A pellet with a 2.4 cm diameter and 6 mm thickness was prepared by pressing the $Y_2O_2S:Eu^{3+}$ powder for 1 h at a pressure of 1.96×10^7 mbar. The pellet was then annealed for 3 h at 600 °C temperature in an open-air furnace to improve its hardness.

2.2. Pulsed Laser Deposition (PLD)

The Si (100) wafers used as substrate were first cleaned using ethanol, followed by methanol each for 10 min in a ultrasonic bath. This was followed by rinsing the substrate in distilled water also for 10 min in a ultrasonic bath. The cleaned substrate was then dried in an oven for 2 h. The deposition chamber was evacuated to a base pressure of 8×10^{-6} mtorr. The Lambda Physic 248 nm KrF excimer laser was used to ablate the phosphor pellet in vacuum and various O_2 partial pressure atmospheres. A Baratron Direct (Gas Independent) PressureVacuum capacitance Manometer (1.33×10^{-2} mtorr) was used for the high pressure measurements. The laser energy density, number of pulses and laser frequency were set to 0.74 J/cm^2, 12,000 and 10 Hz respectively. The substrate temperature was fixed at 300 °C, and the target to substrate distance was 5 cm. The ablated area was 1 cm^2. The Shimadzu Superscan SSX-550 system was used to collect the Scanning Electron Microscopy (SEM) micrographs. Atomic Force Microscopy (AFM) micrographs were obtained from the Shimadzu SPM – 9600 model. X-ray diffraction (XRD) data was collected by using a SIEMENS D5000 diffractometer using CuKα radiation of $\lambda = 1.5405$ nm. PL excitation and emission spectra were recorded using a Cary Eclipse fluorescence spectrophotometer (Model: LS 55) with a built-in xenon lamp and a grating to select a suitable wavelength for excitation. The excitation wavelength was 230 nm and the slit width was 10 nm. The afterglow curves for the films were also obtained with the Cary Eclipse spectrophotometer.

3. Results and discussion

3.1. X-ray diffraction

Fig. 1 shows the XRD patterns of $Y_2O_2S:Eu^{3+}$ thin films grown at 300 °C in vacuum atmosphere as well as in various oxygen partial pressures. The patterns show mixed phases of cubic and hexagonal crystal structures. The films grown at low and high oxygen partial pressure are predominantly cubic, while that grown at moderate pressure (100 mtorr) is predominantly hexagonal. The average lattice parameters for hexagonal phase $a = 3.785$ nm and $c = 6.589$ nm, are very close to the standard values provided in the powder diffraction file PDF #24-1424. The intensities of the XRD peak from the (100) and (113) crystal planes were found to increase with the oxygen partial pressure in the range from 20 to 140 mtorr O_2. This may be attributed to the enhanced oxidation kinetics and improvement in crystalline nature of the films. As the oxygen partial pressure increase, the crystallinity of the films improved. It is also clear that the 300 °C thin film consist of nanoparticles as seen from the broad XRD peaks. The estimated crystallite size of the films with hexagonal and cubic phase ranging between 50 and 70 nm and is shown in Fig. 2.

It is observed that for the $Y_2O_2S:Eu^{3+}$ nanostructures, there is a marginal decrease (−0.26%) in crystallographic unit-cell that tends to contract due to the increase in surface area of the deposited film as compared to that of the substrate itself. This may have been caused by stress between the two surfaces and may lead to a decrease in the lattice constant. Eu_2O_3 diffraction peaks

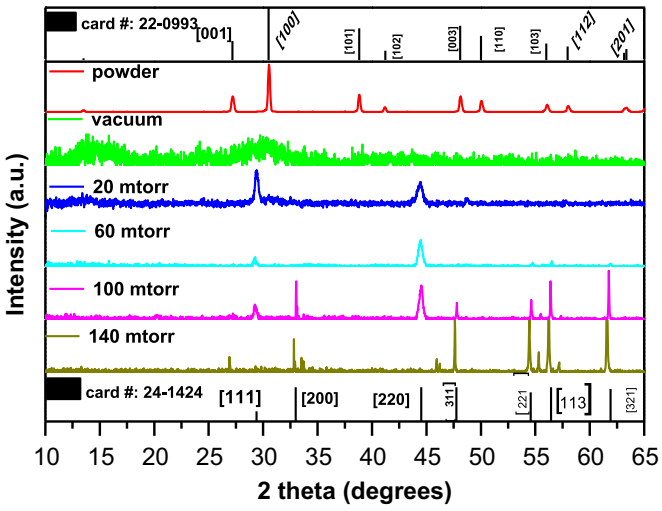

Fig. 1. X-ray diffraction patterns of films deposited in vacuum and various O_2 partial pressures and the standards JCPDS card nos: 24-1424 and 22-0993.

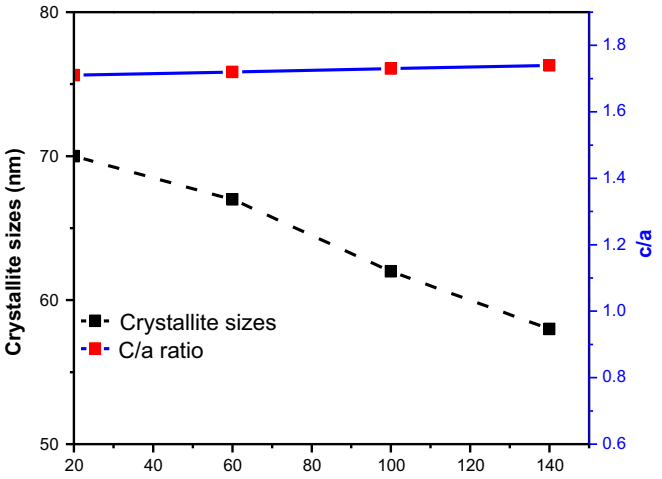

Fig. 2. Crystallite sizes and axial ratio as functions of oxygen partial pressure.

from XRD patterns were not detected indicating that the Eu^{3+} was incorporated into the Y_2O_2S host lattice homogeneously [18].

Fig. 2 shows the role of oxygen partial pressure on crystallite sizes and axial ratio. A monotonous increase of the axial ratio (c/a) and decreasing particle size is established by means of X-ray analysis for a series of thin films deposited at vacuum as well as various oxygen ambient. It is shown that the effect cannot be explained by impurity or intrinsic defects in the thin films. The relations obtained are based on the size dependence of the internal stress and the intra-crystalline pressure stipulated by the interaction of the elements of the crystal charge lattice. Calculations made for the ion charge lattice of quartz agrees with the monotonous increase of the lattice parameters with decreasing particle size.

3.2. Morphology

Fig. 3 shows the SEM images for $Y_2O_2S:Eu^{3+}$ thin films ablated in (a) vacuum, (b) 20 mtorr, (c) 100 mtorr and (d) 140 mtorr oxygen ambient, at 300 °C and fluence of 1.6 ± 0.1 J cm^{-2}. The thin film ablated in vacuum and 20 mtorr O_2 show rougher layers. A smoother surface is however visible from the films ablated in 60 mtorr O_2 and it appears as a layer consisting of spherically shaped nano-particle layer in all the images. The film deposited in

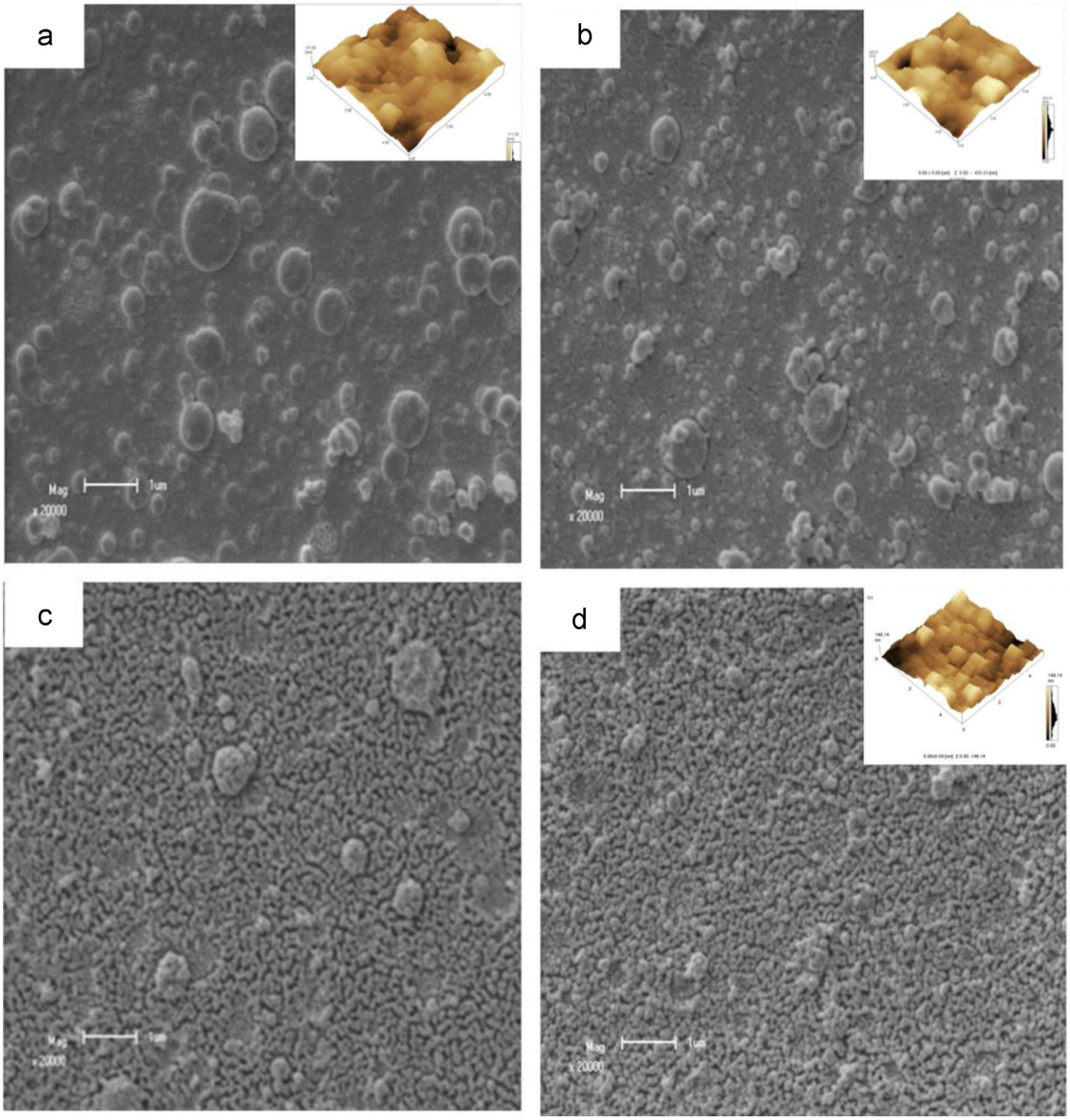

Fig. 3. SEM images of the thin films ablated in (a) vacuum, (b) 20 mtorr, (c) 60 mtorr and (d) 140 mtorr O_2 ambient at 300 °C with a fluence of 0.767 ± 0.1 J cm-2 (5 kV beam energy, magnification of × 20,000 and a scale of 1 μm (FOV: 2 × 1 μm). As insets: 3D height AFM images done in contact mode for the thin films ablated in (a) vacuum, (b) 20 mtorr and (c) 140 mtorr oxygen ambient.

140 mtorr ambient show some layer on the substrate which is even smoother than that in figure (c) as shown in figure (d). The size distribution was broad and the average diameter was about 60 ± 0.5 nm. The existence of bigger micron size particles also occur on all the thin films. These bigger micron particles can severely degrade the performance of electronic and optical devices and elimination can be done by optimization of the process parameters [19]. These SEM images give a rough indication of the surface morphology but better imaging was obtained with AFM analysis.

3.3. Atomic Force Microscopy (AFM)

Fig. 3 also shows AFM images of the samples deposited in (a) vacuum, (b) 20 mtorr and (c) 140 mtorr as insets. It is clear that almost hexagonally-shaped nanoparticles were deposited during the deposition process. The particle sizes of the different films varied from 60 to 70 nm depending on the oxygen partial pressure. An average particle size of 70 nm was calculated for the film grown at 20 mtorr, 300 °C, and the particle size of 58 nm was calculated for the film grown at 140 mtorr, 300 °C. The particles were also less agglomerated at the higher oxygen partial pressures. The mean free path of the particles in a low ambient pressure is longer compared to the mean free path at higher ambient pressures.

More collisions between the ultrafine particles (vaporized particles close to the target) at a higher ambient pressure lead to nucleation and growth of smaller nanoparticles when arriving at the substrate. In vacuum there are virtually no collisions between the particles before reaching the substrate. Longer residence time of the particles in the plume, as is the case at higher ambient pressures, lead to more evenly distributed particles. Light emission from the spherical shaped phosphor particles as excited by the electron beam is more intense due to the fact that much less photons encounter total internal reflection [20]. The increase in the deposition pressure is reported to have caused an increase in

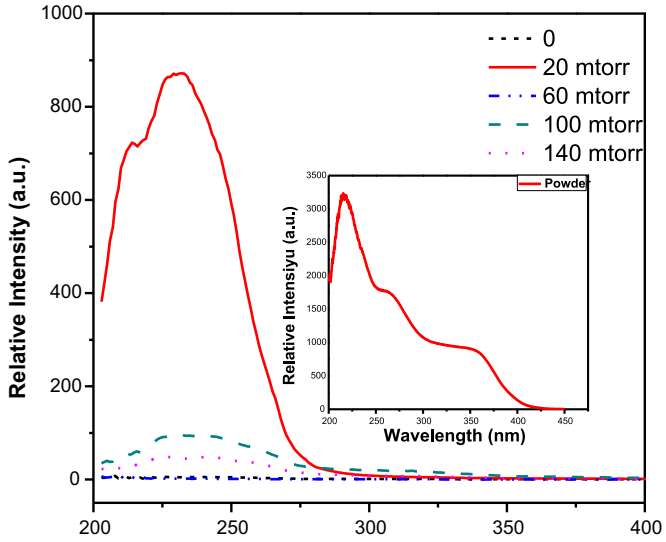

Fig. 4. Excitation spectra for films deposited in vacuum and at different oxygen partial pressure. The inset show excitation spectrum of $Y_2O_2S:Eu^{3+}$ powder phosphor.

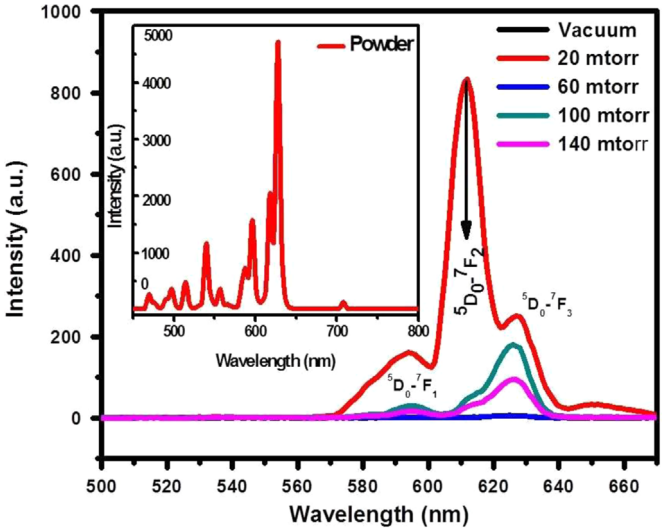

Fig. 5. Emission spectra for films deposited in vacuum and at different oxygen partial pressure. The inset shows emission spectrum of $Y_2O_2S:Eu^{3+}$ powder phosphor. (For interpretation of the references to color in this figure legend, the reader is referred to the web version of this article)

the connectivity (agglomeration) between particles due to sintering of small particles [21]. This would eventually lead to grain growth at high enough pressure. In this case, we also found that more agglomeration occurred at higher oxygen partial pressure.

3.4. Photoluminescence spectra

Fig. 4 indicates the excitation spectra of $Y_2O_2S:Eu^{3+}$ thin films as well as Y_2O_2S; Eu^{3+} powder (inset). Excitation spectra were recorded keeping the emission wavelength at 619 nm. These spectra consist of several excitation bands of the f–f transitions, which are ascribed to different transitions from ground state $^5D_0$ to the various excitation states of ^5D_J (J=1,2,3 and 4) electronic configuration of the Eu^{3+} ions.

Fig. 5 shows the emission spectra of Y_2O_2S: Eu^{3+} thin films and $Y_2O_2S:Eu^{3+}$ powder (inset) red-emitting phosphor. Films deposited in vacuum and those deposited at different oxygen partial pressures as well as the powder $Y_2O_2S:Eu^{3+}$ were used for the PL spectrum measurements. All the samples were excited at a wavelength of 230 nm. For the powder sample, the PL emission spectra consist of several peaks corresponding to different energy transitions of the $Y_2O_2S:Eu^{3+}$ phosphor. Totally, there are three groups of distinctive emission peaks between 590 and 629 nm, which are related to the $^5D_0$–^7F_J (J=1,2,3) transitions of Eu^{3+}, respectively. In the case of the thin films the PL reveals three peaks only which are assigned to $^5D_0$–$^7F_1$, $^5D_0$–$^7F_2$ and $^5D_0$–$^7F_3$ transitions of Eu^{3+} ions. The strongest emission peak for all these samples both thin films and powder $Y_2O_2S:Eu^{3+}$ is from the $^5D_0$–$^7F_2$ transition of Eu^{3+}. The fact that the dominant emission is from the parity forbidden electric dipole transition rather than from the magnetic dipole transition ($^5D_0$–$^7F_1$) indicates that Eu^{3+} is located at the site with no inversion symmetry in the Y_2O_2S lattice (C_2 site) [22]. Compared with the $^5D_0$–$^7F_2$ transition, the intensity of the $^5D_0$–$^7F_1$ transition corresponding to the orange color is much lower, which makes the deposited $Y_2O_2S:Eu^{3+}$ a purer red phosphor. This is also confirmed by the inset of Fig. 5, which shows that the PL emission intensity of the powder is more than 6 times higher than the intensity of $Y_2O_2S:Eu^{3+}$ thin films.

The reason behind observing the intense red emission from $Y_2O_2S:Eu^{3+}$ in the case of hexagonal and also cubic phase can be understood by considering the structure of Y_2O_2S. The coordinate number of Y_2O_2S is twelve and forms hexagonal structure with two different sites (C_2 and C_{3i}) for rare-earth (RE) ions substitution. The C_2 is a low symmetry site without an inversion center whereas C_{3i} is a high symmetry site having an inversion center. When Eu^{3+} is located at a low symmetry (C_2), the red emission is dominant whereas the orange emission is dominant when Eu^{3+} is located at high symmetry (C_{3i}). In the present case, red emission is dominant suggesting that the location of Eu^{3+} is more favorable at C_2 site. As the C_2 site does not have an inversion center, electric dipole transition from Eu^{3+} ions attached to this site are more favorable than the magnetic dipole transitions. The similarity of the ionic radii of Eu^{3+} and Y^{3+} ions for both hexagonal as well as cubic phase allows the easy substitution of Y^{3+} ions with Eu^{3+} ions at C_2 sites giving rise to intense red emission in all the samples. The emission peaked at 590 nm due to $^5D_0$–$^7F_1$ transition of Eu^{3+} is quenched at higher O_2 partial pressure. The most intense peak at 619 nm due to $^5D_0$–$^7F_2$ transition is totally quenched at higher O_2 partial greater than 20 mtorr. Similarly, the peaks at 630 nm due to $^5D_0$–$^7F_3$ transition are quenched at higher O_2 pressure. In the case of vacuum atmosphere as well as 60 mtorr O_2 partial pressure, the peaks are not visible in all the three transitions, while 20 mtorr O_2 partial pressure provides the highest intensity at all the transitions. This can be explained by visiting the oxidation states or kinetics of the Eu^{3+} ions. The most intense peak at 619 nm is assigned to the $^5D_0$–$^7F_2$ transition for 20 mtorr O_2 partial pressure confirms the presence of Eu^{3+}, making 20 mtorr to have highest intensity in all three transitions.

Fig. 6 shows a plot of maximum peak intensity as a function of oxygen partial pressure. The figure indicates that the maximum peak intensity initially increases monotonously between 0 mtorr and 20 mtorr, then decreased at higher oxygen partial pressure. The optimum luminescence intensity was achieved at 20 mtorr due to the fact that possible oxidation of Eu^{3+} to Eu^{2+} did not take place at this particular O_2 partial pressure. This optimum value of 20 mtorr O_2 partial pressure can be utilized in future research but under different deposition conditions.

3.5. Afterglow decay curves of the red phosphors

The afterglow properties of thin films ablated at vacuum and various oxygen pressures are compared, as shown in Fig. 7. It can be seen that the decay curve of the film ablated at 20 mtorr has highest afterglow and brightness, while the film ablated in

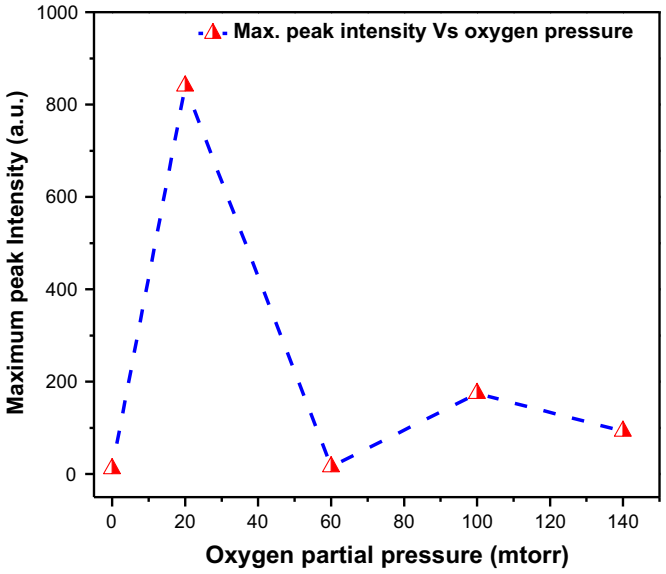

Fig. 6. The plot of maximum peak intensity versus oxygen partial pressure.

vacuum and 60 mtorr has the lowest afterglow and brightness. This indicates that vacuum and lower oxygen pressure favors long afterglow and higher intensities and vice versa. The decay times of the phosphor can be estimated by using the following double exponential equation;

$$I = A_1\exp(-t/\tau_1) + A_2\exp(-t/\tau_2)$$

where I is the phosphorescence intensity, A_1, and A_2, are constants, t is the time, τ_1 and τ_2, are decay times for exponential components, respectively. The fitting results of parameters t_1 and t_2 are listed in Table 2 below and the expected experimental error is ± 0.0017 m/s. (Table 1 and 2).

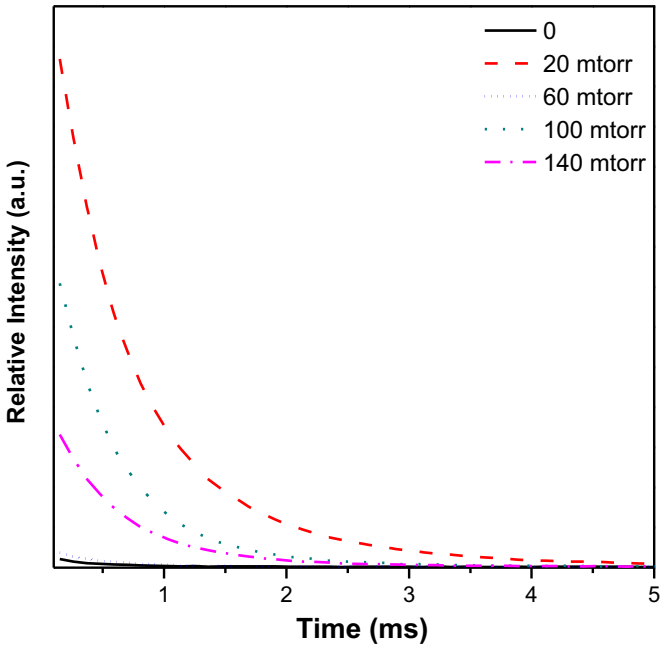

Fig. 7. Decay curves for the thin films deposited in vacuum atmosphere and at different oxygen ambient.

Table 1
Showing how oxygen partial pressures affect lattice parameters and particle size of the films.

O_2 partial pressure (mtorr)	Lattice parameters			Particle size (nm)
	Hexagonal		Cubic	
	a	c	a	
Vacuum	–	–	–	–
20	3.805	6.650	3.789	70 ± 0.5
60	3.798	6.642	3.785	67 ± 0.5
100	3.786	6.633	3.781	62 ± 0.5
140	3.745	6.596	3.776	58 ± 0.5

Table 2
Decay constants for the fitted decay curves of the thin films ablated in vacuum and various oxygen partial ambient.

O_2 pressure (mtorr)	Vacuum	20	60	100	140
Components (ms)	Decay constants (τ, s)				
Fast (τ_1)	0.346	0.400	0.352	0.388	0.372
Medium (τ_2)	0.542	0.600	0.558	0.597	0.582

3.6. Optical properties

3.6.1. Absorbance spectra

The UV–vis reflectance spectra of the samples are given in Fig. 8. The spectra of all the samples show good optical quality in the visible range due to reflectance in the 200–500 nm range. The sharp absorption edge is characteristic of a homogeneous structure [23]. The figure shows that the absorption edge shifted to higher wavelength for lower O_2 partial pressure and then reduced to lower wavelength for higher O_2 partial pressure. Furthermore, absorption bands corresponding to the forbidden Eu^{3+} 4f–4f transitions were detected for higher O_2 partial pressure. The band at around 344 nm is attributed to the exciton absorption, which is red-shift compared with powder $Y_2O_2S{:}Eu^{3+}$ [24]. The absorption peaks at around 290 and 340 nm are assigned to $^5D_0$–$^7F_1$and $^5D_0$–$^7F_2$ transitions of Eu^{3+} ions, respectively [25].

3.6.2. Determination of band gap from reflectance spectra

The Kubelka–Munk equation was used to calculate the band gap of the as-deposited thin film using a diffuse reflectance

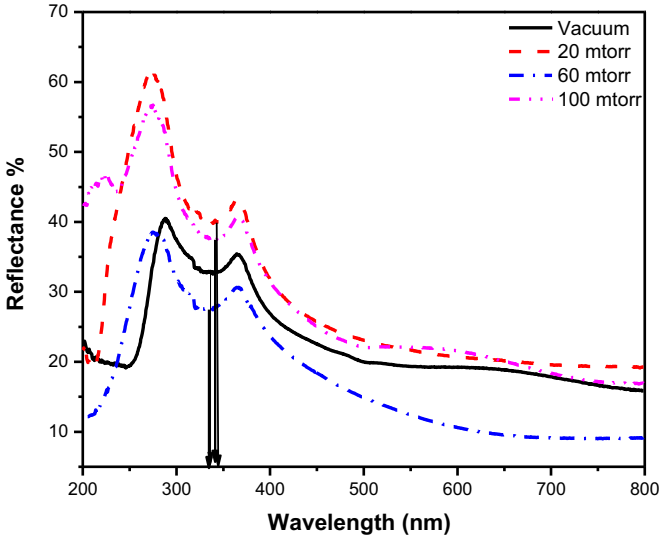

Fig. 8. UV–vis diffuse reflectance spectra of nanocrystalline $Y_2O_2S{:}Eu^{3+}$ thin film deposited in vacuum and different oxygen pressure.

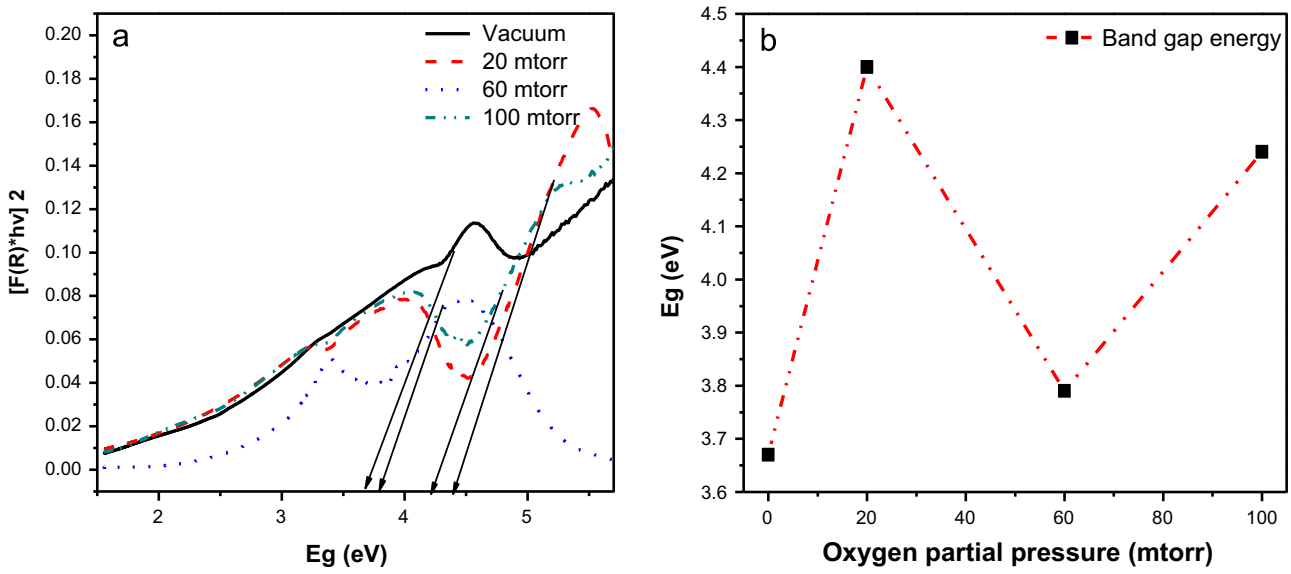

Fig. 9. (a) Graph of $F[(R)*hv]^2$ as a function of band gap energy, (b) dependance of band gap energy on partial oxygen pressure.

spectrum. On the other hand, the band gap (Eg) and absorption coefficient α of the indirect band gap semiconductor is related through the well-known Tauc relation. The average Eg value for the thin films was found to be 4.03 eV, which is almost in agreement with the literature values by other researchers [26,27]. The observed optical band gap for Y_2O_2S: Eu^{3+} thin films has increased to 4.24 eV as the O_2 partial pressure increased to 100 mtorr as shown in Fig. 9(a). The change in optical band gap values may also be due to the change of crystal structure of the Y_2O_2S thin films. This is also confirmed by the fact that the PL emission intensity of the powder is more than 6 times greater than the intensity of Y_2O_2S:Eu^{3+} thin films.

The dependence of the band gap energy of the Y_2O_2S on the O_2 partial pressure is shown in Fig. 9(b). It can be seen from this graph that the band gap of the Y_2O_2S; Eu^{3+} thin films increased with the amount of O_2 partial pressure except for film deposited in 60 mtorr ambient. The decrease in the band gap energy and the shift of the absorption edges to higher wavelengths might be due to the presence of defect states and disorder due to the O_2 partial pressure [28–30]. The O_2 partial pressure might have introduced new states close to the conduction band of the Y_2O_2S:Eu^{3+}. A new defect band is therefore formed below the conductions which lead to reduction in the effective band gap [31,32]. It is clear that at 20 mtorr O_2 partial pressure the estimated band gap increased to 4.40 eV.

4. Conclusion

Y_2O_2S:Eu^{3+} thin films were successfully grown onto the Si (100) substrates at different oxygen ambient. XRD show mixed phases of cubic and hexagonal crystal structures. The films grown at low and high oxygen partial pressure are predominantly cubic, while that grown at moderate pressure (100 mtorr) is predominantly hexagonal. The thin films were composed of nanoparticles. The size of the particles depended on the oxygen partial pressure. The decrease in the oxygen partial pressure resulted into big particles which are actually piling up of smaller particles and therefore a rougher surface. The PL measurements showed red emission of Y_2O_2S:Eu^{3+} thin films as well as the powder Y_2O_2S: Eu^{3+} with the most intense peak appearing at 619 nm, which is assigned to the $^5D_0$–$^7F_2$ transition of Eu^{3+}. This intense peak is quenched at higher O_2 partial pressure greater than 20 mtorr. The emission peak at 590 nm due to $^5D_0$–$^7F_1$ transition of Eu^{3+} is also quenched at higher O_2 partial pressure. UV–vis measurement revealed an average band gap of 4.03 eV.

Acknowledgment

This project is supported by Africa Laser Center (ALC) (Grant number LHIK 500 task ALC - R011), The South African Research Chairs Initiative of the Department of Science and Technology and University of the Free State, South Africa (UFS). The authors acknowledge their financial support.

References

[1] C.R. Ronda, J. Lumin. 49 (1997) 72.
[2] R. Schmechel, M. Kennedy, H. Von Seggern, J. Appl. Phys. 89 (3) (2001) 1679.
[3] A. Konrad, U. Herr, R. Tidecks, F. Kummer, K. Samwer, J. Appl. Phys. 90 (7) (2001) 3516.
[4] H.S. Peng, H.W. Song, B.J. Chen, S.Z. Lu, S.H. Huang, Chem. Phys. Lett. 370 (2003) 485.
[5] W.W. Zhang, W.P. Zhang, P.B. Xie, M. Yin, J. Colloid Interface Sci. 262 (2003) 588.
[6] Y.Q. Zhai, Z.H. Yao, S.W. Ding, M.D. Qiu, J. Zhai, Mater. Lett. 57 (2003) 2901.
[7] H.S. Peng, H.W. Song, B.J. Chen, S.Z. Lu, S.H. Huang, Chem. Phys. Lett. 370 (2003) 485.
[8] T. Hirai, Y. Asada, I. Komasawa, J. Colloid Interface Sci. 276 (2004) 339.
[9] J. Hao, S.A. Studenikin, M. Cocivera, J. Lumin. 93 (2001) 313.
[10] L.P. Wang, G.Y. Hong, Mater. Res. Bull. 35 (2000) 695.
[11] J.P. Lang, X.Q. Xin, J. Solid State Chem. 108 (1994) 118.
[12] H.T. Cui, G.Y. Hong, H.P. You, J. Colloid Interface Sci. 252 (2002) 184.
[13] R.K. Singh, J. Narayan, Phys. Rev. B 41 (1991) 8843.
[14] A. Gupta, in: D.B. Chrisey, G.K. Hubbler (Eds.), Pulsed Laser Deposition of Thin Films, Wiley, New York, 1994, p. 265.
[15] A. Greer, M. Tahal, Mater. Res. Soc. Symp. Proc. 341 (1994) 87.
[16] S.S. Yi, J. Korean Phys. Soc. 45 (2004) 1625.
[17] J. Seon, B. Kyoo, S. Shim, B.K. Moon, S.B. Kim, J.H. Jeong, S.S. Yi, J.H. Kim, J. Korean Phys. Soc. 46 (2005) 1193.
[18] W. Kang, J. Park, D.-K. Kim, K.S. Suh, Bull. Korean Chem. Soc. 22 (2001) 921.
[19] L. Chen, Particles generated by pulsed laser ablation, in: D.B. Chrisey, G. K. Hulber (Eds.), Pulsed Laser Deposition of Thin Films, John Wiley & Sons, Inc., New York, 1994, p. 184.
[20] S. Yi, J.S. Bae, B.C. Choi, K.S. Shim, H.K. Yang, B.K. Moon, J.H. Jeong, J.H. Kim, Opt. Mater. 28 (2006) 703.
[21] S. Erdei, B. Jin, F.W. Ainger, A.S. Bhalla, B. Keszei, J. Vandlik, A. Suveges, J. Appl. Phys. 79 (1996) 2834.
[22] H. Zhang, J. Liu, J. Wang, C. Wang, L. Zhu, Z. Shao, X. Meng, X. Hu, Opt. Lasers Eng. 38 (2002) 527.
[23] V. Buissette, A. Huignard, T. Gacoin, J.-P. Boilot, P. Aschehoug, B. Viana, Surf.

Sci., 532–535, (2003) 444.
[24] R.W.G. Wyckoff, Crystal Structures, 3, Interscience, New York (1963), p. 17.
[25] L.D. Sun, C. Qian, C.S. Liao, X.L. Wang, C.H. Yan, Solid State Commun. 119 (2001) 393.
[26] J.C. Park, H.K. Moon, D.K. Kim, S.H. Byeon, B.C. Kim, K.S. Suh, Appl. Phys. Lett. 77 (2000) 2162.
[27] O.A. Lopez, J. McKittrick, L.E. Shea, J. Lumin. 71 (1) (1997) 197.
[28] S.H. Byeon, K.G. Ko, J.C. Park, D.K. Kim, Chem. Mater. 14 (2002) 603.
[29] G. James, J. Vac. Sci. Technol. A, Vac. Surf. Films 13 (1995) 1175.
[30] C. Misbra, J.K. Berkowitz, K.H. Johnson, P.C. Schmidt, Phys. Rev. B 45 (1992) 10902.
[31] O.A. Lopez, J. Mckittrick, L.E. Shea, J. Lumin. 71 (1997) 1.
[32] D. Hommel, H. Hartmann, J. Cryst. Growth 72 (1985) 346.